Dollinger, Christoph ; Balaresque, Nicholas ; Gaudern, Nicholas ; Gleichauf, Daniel ; Sorg, Michael ; Fischer, Andreas

IR thermographic flow visualization for the quantification of boundary layer flow disturbances due to the leading edge condition

Journal Article	as:	peer-reviewed accepted version (Postprint)
DOI of this document*(secondary publication):		https://doi.org/10.26092/elib/3317
Publication date of this document:		13/09/2024

* for better findability or for reliable citation

Recommended Citation (primary publication/Version of Record) incl. DOI:

Christoph Dollinger, Nicholas Balaresque, Nicholas Gaudern, Daniel Gleichauf, Michael Sorg, Andreas Fischer, IR thermographic flow visualization for the quantification of boundary layer flow disturbances due to the leading edge condition, Renewable Energy, Volume 138, 2019, Pages 709-721, ISSN 0960-1481, https://doi.org/10.1016/j.renene.2019.01.116.

IR thermographic flow visualization for the quantification of boundary layer flow disturbances due to the leading edge condition

Christoph Dollinger [a], Nicholas Balaresque [b], Nicholas Gaudern [c], Daniel Gleichauf [a, *], Michael Sorg [a], Andreas Fischer [a]

[a] University of Bremen, Bremen Institute for Metrology, Automation and Quality Science, Linzer Str. 13, 28359, Bremen, Germany
[b] Deutsche WindGuard Engineering GmbH, Überseering 7, 27580, Bremerhaven, Germany
[c] Anakata Wind Power Resources Ltd., Unit 4 Centre Mead/Osney Mead, Oxford, UK

Keywords:
IR thermographic flow visualization
Boundary layer measurement
Wind turbine rotor blades
Leading edge contamination
Leading edge erosion
Annual energy production

1. Introduction

The leading edge roughness of aerodynamic profiles has a direct effect on the boundary layer flow, and thus effects the aerodynamic performance [1]. Due to the long-term operation under harsh conditions, wind turbine rotor blades suffer from soiling (build-up of ice and contamination with dirt and insects) [2] as well as rain, ice, sand or salt erosion [3–5] of the leading edge, which can cause a premature laminar-turbulent transition of the boundary layer flow [6,7]. Although the leading edge condition (LEC) has long been known to have a significant effect on the aerodynamic properties of airfoils and wind turbine performance [8–11], a measurement method for the quantification of the boundary layer flow impact of the LEC in operation is missing.

Currently, there is no practical method to prevent the contamination of a rotor blade. Even though there are ways to clean the rotor blades, the common method to deal with contamination is to wait for rain to avoid the costly downtime necessary for manual cleaning [3]. In addition, research is being conducted in the aerospace sector in to special surface coatings that reduce the adhesion of dead insects [12], but these approaches are not available in the wind industry so far. One well-established technique to combat leading edge erosion is to install a leading edge protection tape [13]; however, leading edge protection systems also wear over time and the application of protection tapes influences the boundary layer flow due to protuberances and steps [14].

Conventional flow measurement methods such as pressure measurements [15], oil flow [16] or tuft [17] visualization are not suitable for a quantification of the LEC on wind turbines in operation because they are invasive and impact the flow in the same way as erosion (holes for pressure taps) or contamination (oil accumulation and tufts) would. As a quantification of the boundary layer flow impact of the LEC on wind turbines in operation is not

* Corresponding author.
E-mail addresses: c.dollinger@bimaq.de (C. Dollinger), n.balaresque@windguard.de (N. Balaresque), nicholasg@anakatawindpower.com (N. Gaudern), d.gleichauf@bimaq.de (D. Gleichauf), m.sorg@bimaq.de (M. Sorg), andreas.fischer@bimaq.de (A. Fischer).

possible to date, estimates of the resulting impact on power performance are based on simulations or model assumptions of the leading edge condition and subsequently performed wind tunnel measurements [1,18]. Typical industry practice to determine the aerodynamic impact of a contaminated or eroded leading edge is to conduct wind tunnel measurements with and without a tripped boundary layer flow (achieved by applying zig-zag tape) or *Xfoil* flow simulations with transition prescribed close to the leading edge; however, these methods are idealized and only consider two extreme conditions (binary solution). Furthermore, the actual impact on the aerodynamic properties due to the LEC can be significantly higher than due to tripping [7,11].

A non-invasive measurement method is required that enables a quantification of the actual impact of the LEC on the boundary layer flow. This would allow more realistic estimations of losses in annual energy production (AEP) beyond the commonly used binary statement.

A non-invasive measurement of the boundary layer flow state can be performed by thermographic flow visualization. The thermographic flow visualization relies on an initial temperature difference between the measured object and the fluid. The object surface temperature depends on the local heat transfer coefficient between the rotor blade and the incoming flow. The heat transfer coefficient is a function of the surface friction in the different areas of the boundary layer flow [19,20].

Thermographic measurements for flow visualization purposes have been established in wind tunnel experiments for decades to visualize the boundary layer state in ultra- and hypersonic as well as in trans- and subsonic flows [21]. To increase the sensitivity, the aerodynamic profile is usually heated [22,23] or the flow is cooled [24,25]. By doing this, a measurable temperature difference of several Kelvin - and thus a suitable signal-to-noise ratio (SNR) between different flow states - can be observed. In wind tunnel experiments the position of the laminar-turbulent transition as well as areas with laminar or turbulent flow separation can be visualized [26,27]. A new focus is also on extended evaluation methods for increasing sensitivity in challenging applications [28–31]. Outside the wind tunnel, thermographic measurements for the localization of the laminar-turbulent transition in flight experiments on aircraft wings [32], helicopter rotors [33] and wind turbine rotor blades in operation [34] are reported. A thermographic study on the influence of leading edge roughness has been carried out by Ehrmann et al. in wind tunnel experiments; however, the evaluation was performed visually, which resulted in uncertainties of 10% of the chord length in the case of a transition with turbulence wedges due to erosion or contamination of the leading edge [10]. Furthermore, Traphan et al. recently published results for a remote surface damage detection technique based on thermography [35]. A quantitative investigation of the boundary layer flow impact of the LEC on operating rotor blades is missing and the calculations of the resulting losses in AEP are still based on the binary states of a clean and fully tripped rotor blade.

The objectives of this work are firstly, the non-invasive determination of the extent of the boundary layer flow influenced by the LEC with low measurement uncertainty, and secondly, to provide a more realistic estimation of the AEP loss due to the LEC, as an alternative to the current industrial standard.

The measurement approach to determine the extent of boundary layer flow influenced by the LEC as well as the respective impact on the AEP is presented in Sect. 2.1. The approach is demonstrated by measurements on the rotor blades of a 1.5 MW *General Electric* (*GE*) horizontal axis wind turbine with a rotor diameter of 77 m. Both the experimental and the numerical setup are described in Sect. 3, and the field measurement results with respect to the LEC influence on the laminar flow region are presented in Sect. 4. The results of the AEP calculation are reported in Sect. 5. The article closes with conclusions and an outlook on ongoing research questions in Sect. 6.

2. Measurement principle and measurement uncertainty

The measurement approach for the non-invasive determination of the extent of the boundary layer flow influenced by the LEC is based on the thermographic determination of the laminar-turbulent transition location. The procedure for determining the extent ξ_{tr} of influenced boundary layer flow is described in Sect. 2.1. The measurement results enable an estimation of the reduction of the AEP based on a blade element momentum (BEM) simulation model, which is explained in Sect. 2.2.

2.1. Measurement of the influenced laminar flow by the LEC

The LEC influences the boundary layer flow and thus the position of the laminar-turbulent transition. This correlation is used to introduce a non-invasive indication of the LEC in the form of the extent ξ_{tr} of laminar boundary layer flow influenced by erosion and contamination. In order to quantify ξ_{tr}, the positions $P_{tr,nat}$ and $P_{tr,act}$ relative to the chord length of the non-influenced natural transition and the LEC-influenced actual transition are compared:

$$\xi_{tr} = 1 - \frac{P_{tr,act}}{P_{tr,nat}}. \tag{1}$$

ξ_{tr} represents the difference between the natural and the actual transition position normalized to the natural transition position. Hence, a ξ_{tr} close to 100 % indicates an almost completely tripped (turbulent) boundary layer flow and a ξ_{tr} of 0 % indicates an actual transition position that matches the approximated position of the natural transition. In contrast to a simple difference between the two positions, which corresponds to the change in the amount of laminar flow, the normalization of the difference to the natural transition position allows a statement regarding the extent of laminar flow influenced by erosion or contamination of the rotor blade.

Thermographic flow visualization measurements at the wind turbine in operation are performed, which is explained further in Sect. 2.1.1. The signal processing for determining the relative actual transition position $p_{tr,act}$ and the relative natural transition position $p_{tr,nat}$ in the image plane is described in Sect. 2.1.2. Both positions are assigned to the rotor blade geometry, resulting in the chord-based transition positions $P_{tr,act}$ and $P_{tr,nat}$, which is explained in Sect. 2.1.3. Finally, a description of the procedure for specifying the measurement uncertainty is provided in Sect. 2.1.4.

2.1.1. Thermographic flow visualization

In order to determine the spanwise actual and natural transition positions, thermographic flow visualization measurements at the wind turbine in operation are performed. Fig. 1 shows an example of a thermographic image of a rotor blade section at the wind turbine in operation. The image shows the suction side of the rotor blade with the flow direction being upwards, as the image is taken when the rotor blade is moving downwards. Due to the absorbed solar radiation, the rotor blade surface is warmer than the flow. The temperature difference between rotor blade and flow results in a distinct temperature pattern due to varying local heat transfer coefficients that correlate with the boundary layer state. The surface areas with a laminar boundary layer flow appear warmer than surface areas with a turbulent boundary layer flow. The transition from laminar to turbulent flow can be determined by a steep

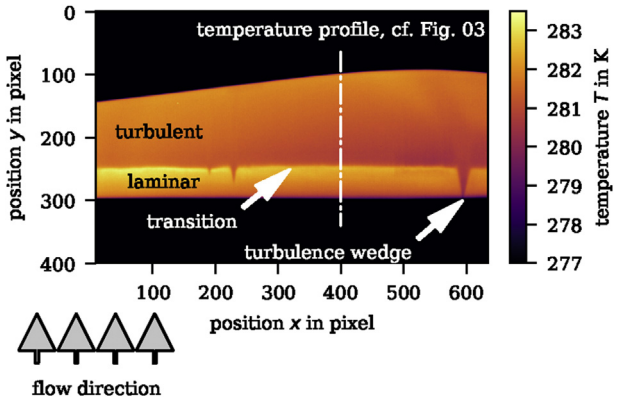

Fig. 1. Thermographic image of a rotor blade section at a wind turbine in operation. Both laminar and turbulent flow can be identified by different surface temperatures due to the local heat transfer coefficients associated with the different flow regimes. Roughness elements can cause a wedge-shaped premature laminar-turbulent transition. The dashed line at $x = 400$ pixels indicates the measured chordwise temperature profile shown in Fig. 3.

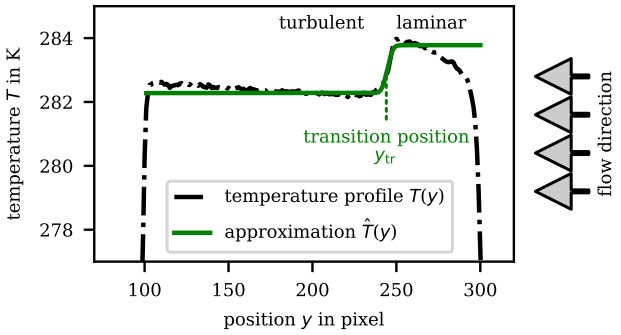

Fig. 3. Measured temperature profile $T(y)$ from Fig. 1 at the position $x = 400$ pixels as well as the corresponding approximated temperature profile $\hat{T}(y)$ with a Gaussian error function. The position y_{tr} of the laminar-turbulent transition can be identified by the sudden change in surface temperature at $y = 245$ pixels.

change in temperature. Surface roughness elements due to erosion or contamination cause local premature laminar-turbulent transitions, which can be identified as turbulence wedges, cf. Fig. 1. The spanwise transition location of the clean blade is considered to be the natural transition position. In the following, the transition position including turbulence wedges is referred to as the actual transition position.

The actual transition position can differ significantly under the same conditions but with a different leading edge roughness. Fig. 2 shows two thermographic images of the suction side of a rotor blade. The images were taken in a time interval of 60 min and clearly show the influence of the LEC on the boundary layer flow. Fig. 2(a) shows the thermographic image of the rotor blade after several days without precipitation. The contamination of the leading edge of the rotor blade is very pronounced and especially in the outer area of the rotor blade almost no laminar boundary layer flow can be identified. The image in Fig. 2(b) was taken immediately after heavy rain, which washed away most of the contamination. The remaining turbulence wedges are either due to particularly persistent soiling or erosion of the rotor blade surface.

2.1.2. Signal processing

The localization of the spanwise laminar-turbulent transition in the thermographic image is found by using an approximation of the temperature profile in the flow direction with a Gaussian error function. The temperature profile at the position $x = 400$ pixels in Fig. 1 and the result of the approximation with the Gaussian error function are shown in Fig. 3. The model function for the approximation is:

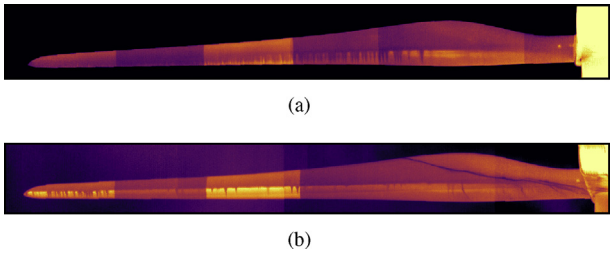

Fig. 2. Thermographic images of an entire rotor blade, with no precipitation falling for a long time period before the image in (a) was taken. The image in (b) was taken directly after heavy rain with a time interval of 60 min to the image in (a).

$$\hat{T} = \hat{a}\,\mathrm{erf}\left(\frac{y - y_{tr}}{\sqrt{2}\,\hat{c}}\right) + \hat{d}. \tag{2}$$

The fit parameter $\hat{a}$ stands for the temperature change in the transition region, y_{tr} is the position of inflexion of the Gaussian error function and the measure for the laminar-turbulent transition position, $\hat{c}$ is the standard deviation (transition width parameter) and $\hat{d}$ is the general temperature offset of the Gaussian error function. The position of the inflexion y_{tr} can be used for an automated evaluation of the thermographic image [26,32,34].

The evaluation of the temperature profile in flow direction enables the localization of the relative actual transition position $p_{tr,act}$ along the span in $j = 1, \ldots, J$ columns of the thermographic image:

$$p_{tr,act} = \frac{1}{J}\sum_{j=1}^{J}\frac{y_{tr,j} - y_{LE,j}}{y_{TE,j} - y_{LE,j}} = \frac{1}{J}\sum_{j=1}^{J} p_{tr,act,j}, \tag{3}$$

with y_{LE} and y_{TE} as the positions of the visible leading edge (LE) and trailing edge (TE), also determined by the approximation of the temperature gradient with the Gaussian error function. The actual transition position $p_{tr,act}$ includes the laminar-turbulent transition shift by turbulence wedges due to erosion or contamination of the rotor blade surface. In order to gain information about the LEC, the natural transition position $p_{tr,nat}$ is additionally determined by a weighted linear least squares fit of the actual transition positions $p_{tr,act,j}$. Due to the weighting, the influence of the wedges is almost completely suppressed and the transition position without turbulence wedges can be approximated. An example for the result of the image processing is shown in Fig. 4 based on the thermographic image presented in Fig. 1.

2.1.3. Geometrical assignment

For the localization of the laminar-turbulent transition with respect to the profile geometry of the rotor blade, a geometric assignment of the two-dimensional image information to the three-dimensional geometry is required. By taking into account the position of the investigated rotor blade section in relation to the camera, the visible surface area of the rotor blade section can be assigned to its geometry. With the known distance and pitch angle, a series of coordinate transformations is carried out to enable the determination of the viewing angle. The consideration of the position of the transition in the image plane of the thermographic image allows the determination of the position on the rotor blade surface and subsequently the projection of this position onto the rotor blade chord.

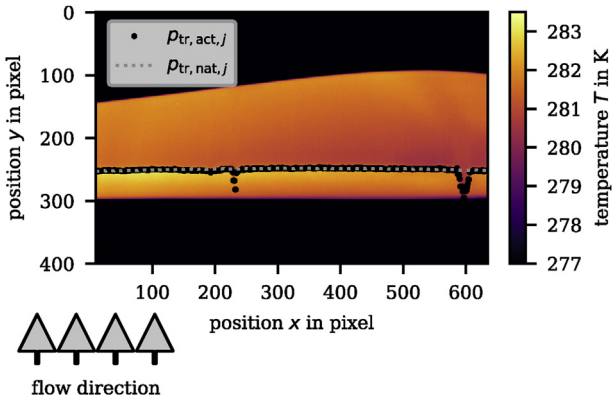

Fig. 4. Example result of the signal processing for the localization of the actual and the natural transition position based on the thermographic image shown in Fig. 1.

For the geometric assignment of the laminar-turbulent transition position (or any other feature in the thermographic image) to the chord, the profile geometry, the position of the profile - defined by the position of the center of rotation and the blade angle Θ of the rotor blade section - as well as the position of the thermographic camera are required. The blade angle Θ follows from the pitch angle ϑ and the twist angle ϑ_t and can be written as

$$\Theta(r) = \frac{1}{2}\pi + \vartheta + \vartheta_t(r) \tag{4}$$

The angle of twist ϑ_t is a function of the radial position r on the rotor radius. The position of the profile of the investigated rotor blade section is now defined in a coordinate system relative to the position of the thermographic camera with the coordinates $[X_i^c, Y_i^c]^T$; therefore, the profile coordinates $[X_i^p, Y_i^p]^T$ are rotated by the blade pitch angle Θ and translated by the measuring distance $[\Delta X, \Delta Y]^T$ between the camera and the center of rotation of the rotor blade section in X and Y direction using a homogeneous transformation matrix [36]:

$$\begin{bmatrix} X_i^c \\ Y_i^c \\ 1 \end{bmatrix} = \begin{bmatrix} \cos(-\Theta) & -\sin(-\Theta) & \Delta X \\ \sin(-\Theta) & \cos(-\Theta) & \Delta Y \\ 0 & 0 & 1 \end{bmatrix} \cdot \begin{bmatrix} X_i^p \\ Y_i^p \\ 1 \end{bmatrix}, \tag{5}$$

with ΔX as the distance between the thermographic camera and the wind turbine tower base and ΔY as the hub height of the wind turbine. This results in the position of the rotor blade profile segment relative to the position of the thermographic camera. Fig. 5 shows the thermographic camera, the wind turbine and the profile of the investigated rotor blade section in the camera coordinate system.

Next, the Cartesian profile coordinates $[X_i^c, Y_i^c]^T$ within the camera coordinate system are transformed into polar coordinates. By that, each profile coordinate can be expressed by the distance from the coordinate origin $r_i^c = \sqrt{(X_i^c)^2 + (Y_i^c)^2}$ and an angle $\varphi_i^c = \arccos\left(\frac{X_i^c}{r_i^c}\right)$. The representation in polar coordinates enables the identification of the two profile coordinates with the minimal and the maximal polar angle φ_{min}^c and φ_{max}^c. These two coordinates are the surface points that can barely be observed from the camera's point of view and thus the chordwise edges of the visible surface area in the thermographic image. The difference between these two angles is therefore the part of the angle of aperture that results in the imaging of the rotor blade surface in the thermographic image.

The image plane positions of the visible leading edge, the visible trailing edge, and the laminar-turbulent transition are known from the previously-executed evaluation of the thermographic image by the presented signal processing (Sect. 2.1.2). The angle φ_{tr}^c at which the laminar-turbulent transition is visible can be determined using the relative position of the transition in the image plane:

$$\begin{aligned} \varphi_{tr}^c &= p_{tr} \cdot (\varphi_{max}^c - \varphi_{min}^c) + \varphi_{min}^c \\ &= \varphi_{min}^c \cdot (1 - p_{tr}) + p_{tr}\, \varphi_{max}^c. \end{aligned} \tag{6}$$

Depending on whether the angle of the line of sight to the visible leading edge or the angle to the visible trailing edge is larger, $p_{tr} = p_{tr}$ or $p_{tr} = (1 - p_{tr})$ has to be assumed, respectively.

The chord of the rotor blade profile is parallel to the X^p-axis within the profile coordinate system, cf. Fig. 5. For this reason the position of the laminar-turbulent transition with respect to the chord can be expressed as the inverse transformed X^p-component of the intercept $[X_S^c, Y_S^c]^T$ of the line of sight to the transition at the transition angle φ_{tr}^c with the rotor blade surface. Generally, the surface coordinates are only available in a discrete resolution; therefore, the surface between the two coordinates whose angles are closest to the transition angle φ_{tr}^c is approximated by a linear function. The polar distance r_{tr}^c of the transition position on the surface of the rotor blade section results in

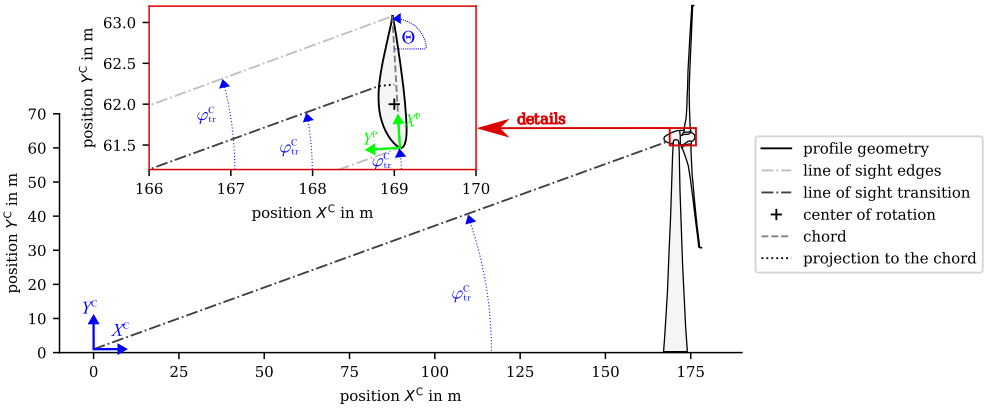

Fig. 5. Example illustration of the measurement situation for field measurements within the camera coordinate system with a distance of $\Delta X = 169$ m to the wind turbine with a hub height of $\Delta Y = 62$ m. The thermographic camera is positioned luvwards and observes the suction side of the rotor blade segment at the position r of the radius R pitched by the rotor blade angle $\Theta = \frac{1}{2}\pi + \vartheta + \vartheta_t(r)$.

$$r_{\mathrm{tr}}^{\mathrm{c}} = \frac{n}{\sin(\varphi_{\mathrm{tr}}^{\mathrm{c}}) - m\cos(\varphi_{\mathrm{tr}}^{\mathrm{c}})}, \tag{7}$$

where m and n are the gradient and the offset of the linear function. The coordinates of the intercept in the Cartesian camera coordinate system can be expressed as:

$$\begin{bmatrix} X_{\mathrm{S}}^{\mathrm{c}} \\ Y_{\mathrm{S}}^{\mathrm{c}} \end{bmatrix} = \begin{bmatrix} r_{\mathrm{tr}}^{\mathrm{c}}\cos(\varphi_{\mathrm{tr}}^{\mathrm{c}}) \\ r_{\mathrm{tr}}^{\mathrm{c}}\sin(\varphi_{\mathrm{tr}}^{\mathrm{c}}) \end{bmatrix} = \begin{bmatrix} \frac{n}{\sin(\varphi_{\mathrm{tr}}^{\mathrm{c}}) - m\cos(\varphi_{\mathrm{tr}}^{\mathrm{c}})}\cos(\varphi_{\mathrm{tr}}^{\mathrm{c}}) \\ \frac{n}{\sin(\varphi_{\mathrm{tr}}^{\mathrm{c}}) - m\cos(\varphi_{\mathrm{tr}}^{\mathrm{c}})}\sin(\varphi_{\mathrm{tr}}^{\mathrm{c}}) \end{bmatrix}. \tag{8}$$

The position X_{tr} of the laminar-turbulent transition is the inverse transformed X^{p}-component of the intercept $[X_{\mathrm{S}}^{\mathrm{p}}, Y_{\mathrm{S}}^{\mathrm{p}}]^{\mathrm{T}}$ in the profile coordinate system:

$$\begin{bmatrix} X_{\mathrm{S}}^{\mathrm{p}} \\ Y_{\mathrm{S}}^{\mathrm{p}} \\ 1 \end{bmatrix} = \begin{bmatrix} \cos(-\Theta) & -\sin(-\Theta) & \Delta X \\ \sin(-\Theta) & \cos(-\Theta) & \Delta Y \\ 0 & 0 & 1 \end{bmatrix}^{-1} \begin{bmatrix} X_{\mathrm{S}}^{\mathrm{c}} \\ Y_{\mathrm{S}}^{\mathrm{c}} \\ 1 \end{bmatrix} \tag{9}$$

Finally, the relative position P_{tr} of the laminar-turbulent transition can be specified by the normalization to the profile chord length c:

$$P_{\mathrm{tr}} = \frac{X_{\mathrm{S}}^{\mathrm{p}}}{c} = \frac{X_{\mathrm{tr}}}{c}. \tag{10}$$

2.1.4. Measurement uncertainty

At first, a Gaussian uncertainty propagation of the thermographic camera noise (uncertainty of the measured temperature T_i) to the transition position y_{tr} is performed. According to the model approximation with respect to the model from Eq. (2), the covariance matrix of the estimator $\underline{\widehat{\theta}}_{\widehat{T}} = [\widehat{a}, y_{\mathrm{tr}}, \widehat{c}, \widehat{d}]$ reads [37]:

$$\mathrm{Cov}\left(\underline{\widehat{\theta}}_{\widehat{T}}, \underline{\widehat{\theta}}_{\widehat{T}}\right) = \left(H^{\mathrm{T}}\, C^{-1}\, H\right)^{-1}, \tag{11}$$

where the second element of the main diagonal yields the square of the position measurement uncertainty $\sigma_{y_{\mathrm{tr}}}$, H is the Jacobian matrix of the model function with the partial derivatives of the model function to all fit parameters at every operating point, and C is the covariance matrix of the uncorrelated values of the temperature profile. The covariance matrix C is a diagonal matrix whose main diagonal is represented by the variance $\sigma_{T_i}^2$ of the temperature T_i. The measurement uncertainty σ_{T_i} of each individual temperature T_i per pixel measured with a thermographic camera can be considered as the combination of detector noise and fixed pattern noise. Both noise sources can be determined by a sequence of measurements of a homogeneously tempered surface with a large sample size L. The detector noise is the mean temporal noise of the temperature measurements:

$$\sigma_{T_{i,\mathrm{detector}}} = \frac{1}{M \cdot N}\sum_{y=1}^{M}\sum_{x=1}^{N}\sqrt{\frac{1}{L-1}\sum_{l=1}^{L}\left(T_{yx}[l] - \overline{T}_{yx}\right)^2}, \tag{12}$$

where $\overline{T}_{yx} = \frac{1}{L}\sum_{l=1}^{L} T_{yx}[i]$ is the average temperature in the measurement sequence $T_{yx}[l], l = 1, \ldots, L$ for each pixel $[y,x]$, $y = 1, \ldots, M$ stands for the image row and $x = 1, \ldots, N$ for the image column. The fixed pattern noise due to a non-uniformity of the individual pixels of the detector can be quantified by a temporal averaging of the measurement sequence and a subsequent evaluation of the spatial noise:

$$\sigma_{T_{\mathrm{pattern}}} = \sqrt{\frac{1}{(M \cdot N) - 1}\sum_{y=1}^{M}\sum_{x=1}^{N}\left(\overline{T}_{yx} - \overline{T}\right)^2} \tag{13}$$

with the overall mean temperature $\overline{T} = \frac{1}{M \cdot N}\sum_{y=1}^{M}\sum_{x=1}^{N}\overline{T}_{yx}$. The temporal averaging reduces the detector noise of each individual pixel by the factor $\frac{1}{\sqrt{L}}$. An estimation of the temperature-dependent photon shot noise has shown that the influence of photon shot noise on the measurement uncertainty of temperature can be neglected for small temperature differences [34]. This allows the assumption $\sigma_{T_i} = \mathrm{const}$ for all measured temperature values T_i on the rotor blade surface.

Validation measurements have shown, that the measurement uncertainty is additionally influenced by flow induced temperature fluctuations [34]. Therefore, the flow induced temperature fluctuations are taken into account in terms of the local standard deviation in the transition region, determined individually for each measurement in the experiments.

The resulting measurement uncertainty $\sigma_{p_{\mathrm{tr,act}}}$ of the relative position $p_{\mathrm{tr,act}}$ of the actual laminar-turbulent transition in the thermographic image according to Eq. (3) results in

$$\sigma_{p_{\mathrm{tr,act}}} = \frac{1}{\sqrt{J}}\sum_{j=1}^{J}\sigma_{p_{\mathrm{tr,act,j}}}. \tag{14}$$

Since there is no correlation between the positions of the visible leading edge y_{LE}, the visible trailing edge y_{TE} and the laminar-turbulent transition y_{tr}, the individual uncertainties of the relative transition position $p_{\mathrm{tr,act},j}$ read

$$\sigma_{p_{\mathrm{tr,act},j}} = \sqrt{\left(\frac{\partial p_{\mathrm{tr,act}}}{\partial y_{\mathrm{tr},j}}\right)^2\sigma_{y_{\mathrm{tr},j}}^2 + \left(\frac{\partial p_{\mathrm{tr,act}}}{\partial y_{\mathrm{LE},j}}\right)^2\sigma_{y_{\mathrm{LE},j}}^2 + \left(\frac{\partial p_{\mathrm{tr,act}}}{\partial y_{\mathrm{TE},j}}\right)^2\sigma_{y_{\mathrm{TE},j}}^2}. \tag{15}$$

In the case of the measurement uncertainty $\sigma_{p_{\mathrm{tr,nat}}}$ for the position $p_{\mathrm{tr,nat}}$ of the natural transition, a manual preselection of the transition positions takes place prior to the calculation of the standard uncertainty of the mean value and positions at turbulence wedges were not considered.

According to Eqs. (3) and (5) to (10), the geometrical assignment of the actual and the natural laminar-turbulent transition position $P_{\mathrm{tr,act}}$ and $P_{\mathrm{tr,nat}}$ to the profile geometry is not only a function of the transition position in the thermographic image but also of the measurement distances ΔX and ΔY in X and Y direction between the thermographic camera and the center of rotation of the rotor blade profile and the rotor blade angle Θ. The uncertainties $\sigma_{P_{\mathrm{tr,act}}}$ and $\sigma_{P_{\mathrm{tr,nat}}}$ can be determined by Monte Carlo simulations taking into account the uncertainties of the mentioned quantities.

The estimation of the measurement uncertainty $\sigma_{\xi_{\mathrm{tr}}}$ of the extent ξ_{tr} of the influenced laminar boundary layer is also carried out with Monte Carlo simulations. The functional relationship is simulated within the uncertainties of $p_{\mathrm{tr,act}}$, $p_{\mathrm{tr,nat}}$, ΔX, ΔY, and Θ:

$$\xi_{\mathrm{tr}} = f\left(p_{\mathrm{tr,act}}, p_{\mathrm{tr,nat}}, \Delta X, \Delta Y, \Theta\right) \tag{16}$$

As the positions of the natural and the actual transition are determined from the same temperature profile measurement data, a correlation of the two position measurements can be assumed. In the measurement uncertainty estimation for ξ_{tr}, the correlation is

not considered because the calculation is simplified and the estimated uncertainty corresponds to a worst case scenario. In fact, the correlation of the transition positions according to the calculation of the difference in Eq. (1) results in a lower measurement uncertainty $\sigma_{\xi_{tr}}$ in reality.

2.2. Estimation of the AEP

For the estimation of the AEP loss due to leading edge erosion and contamination, blade element momentum simulations are carried out. The BEM method is the current industry-standard methodology for analyzing the aerodynamic performance of a wind turbine rotor. Although it is a purely 2D methodology, various correction factors are generally applied to account for the breakdown of the 2D assumptions at the root and tip of the rotor blade. As the key area of interest in this study is not greatly affected by 3D flow, the BEM methodology is suitable for the approach.

The BEM method uses lookup tables of the aerodynamic coefficients (typically measured wind tunnel polars) for a small, discrete number of 2D profile cuts along the blade span and iterates towards a solution based on the equations describing the conservation of momentum in an idealized streamtube [38]. The resulting solution includes the distribution of local angles of attack along the blade, by which the distributions of aerodynamic force are determined. In this work, the aerodynamic coefficient lookup tables - in the form of wind tunnel polars - are modified to include the impact of the leading edge condition through the measured shift in the laminar-turbulent transition positions from $P_{tr,nat}$ to $P_{tr,act}$, which typically results in a reduction of the lift coefficient c_L and an increase of the drag coefficient c_D. The coefficient changes are determined through analysis in *Xfoil*, which is a widely used 2D flow simulation software for the estimation of the aerodynamic force coefficients [39].

3. Experimental and numerical setup

In the following, the experimental setup for the thermographic field measurement (Sect. 3.1) and the wind tunnel experiments (Sect. 3.2) as well as the numerical setup for the BEM simulation (Sect. 3.3) are presented.

3.1. Field measurements

The demonstration of the approach is based on the example of a 1.5 MW *General Electric* (*GE*) horizontal axis wind turbine. The hub height of the investigated wind turbine is 62 m and the rotor diameter is 77 m. The specific model (*GE 1.5* sl) is equipped with rotor blades from the supplier *LM Wind Power* with a length of 37.3 m. The rotor blade type *LM 37.3p* is also used on other wind turbines manufactured for example by *Nordex*, *Repower*, *Fuhrländer*, *Leitwind*, *Goldwind* and others. In order to obtain the rotor blade geometry, one rotor blade was dismantled and measured on the ground with several laser distance sensors, where the accuracy was less than 1 mm [40]. The results of the geometric measurement are five radial profile cuts at $r_1 = 10.45$ m, $r_2 = 17.05$ m, $r_3 = 23.55$ m, $r_4 = 30.15$ m, and $r_5 = 36.75$ m. Fig. 6 shows the two-dimensional geometries of the five radial profile cuts. For the protection of the internal knowledge of the rotor blade manufacturer, the geometries in Fig. 6 are not to scale and slightly distorted.

The geometries are used for the manufacturing of wind tunnel models in order to determine the aerodynamic properties and for the geometric assignment of the two-dimensional thermographic imaging data to the rotor blade geometry.

The measurement distance for the field measurements ranges between 110 and 250 m. Fig. 7 shows the measurement setup for the field measurements at a distance of 250 m leeward of the wind turbine tower base on the pressure side of the rotor blades. The

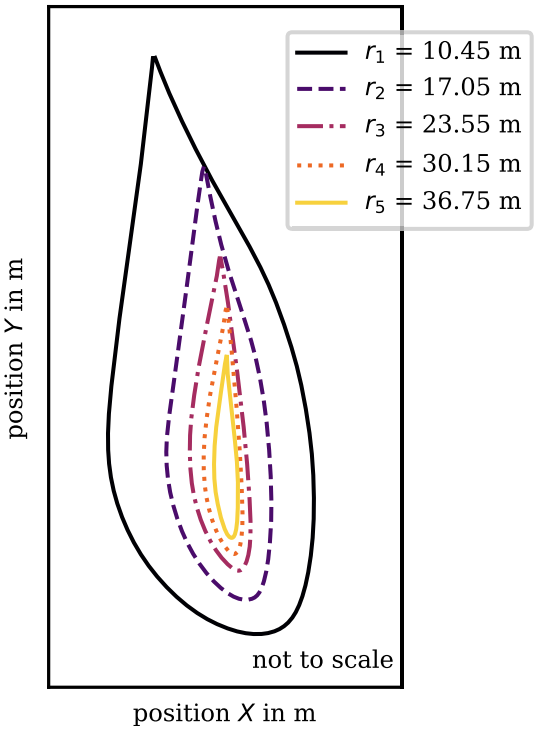

Fig. 6. Individual blade profile cuts of the rotor blade of the type *LM 37.3p* at the radial positions $r_i, i = 1, \ldots, 5$ measured by a laser distance sensors [40].

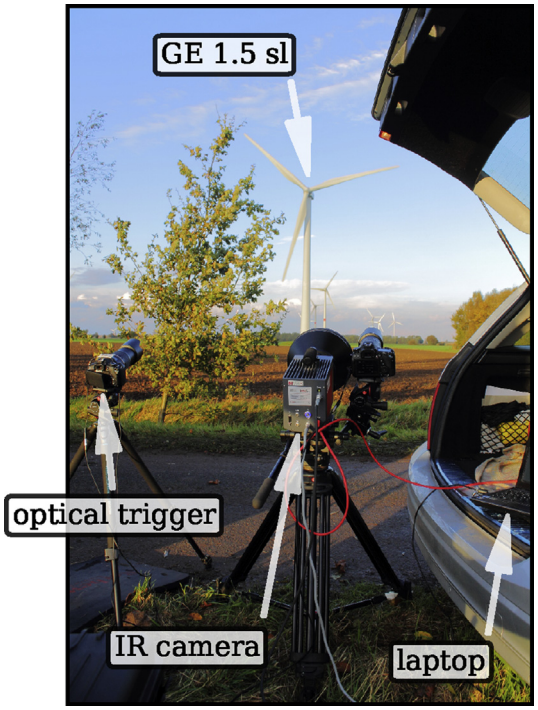

Fig. 7. Experimental setup for the field measurements at the wind turbine in operation. The measurement distance is 250 m leeward of the *GE 1.5* sl wind turbine tower base. The rotor diameter of the wind turbine is 77 m. In the foreground the thermographic camera, an optical trigger and the laptop for the acquisition and evaluation of the images are shown.

field measurements were performed with a cooled thermographic camera with a global shutter (snap-shot detector) from the manufacturer *InfraTec*. The detector is an InSb focal plane array with a format of 640 × 512 pixels (model *ImageIR 8300*). Full-frame resolution images can be acquired at up to 100 Hz sampling frequency. The camera is sensitive between 2 and 5 μm and the noise equivalent temperature difference (NETD) is less than 25 mK @ 30 °C. The dynamic range is 14 bit and the integration time for the acquisition of an image can be set between 1 and 20,000 μs. The camera was calibrated by the manufacturer in a standard calibration routine with measurements of a black body radiator at different temperatures. For the presented measurements a one point non-uniformity correction is performed before each of the measurements. The pixel size in the sensor plane amounts to 15 μm. A 200 mm telephoto lens is used for the field measurements. The lens has an angular aperture of 2.7° × 2.2° and with the given detector size the instantaneous field of view (IFOV) results in 0.08 mrad. This corresponds to a spatial resolution of 8.8–20 mm for the given measurement distances. The thermographic camera is triggered by an optical trigger for the measurements with the wind turbine in operation to enable the acquisition of an image every time one of the blades is passing the camera's field of view. The images are acquired with the camera software development kit (SDK) from the camera manufacturer. The subsequent processing of the images is done in *Python*.

In order to estimate the measurement uncertainty, according to Sect. 2.1.4 and Eq. (16), the uncertainty contributions from the experimental setup are determined. The detector and the fixed pattern noise of the used thermographic camera are determined by a sequence of $L = 500$ measurements of a homogeneously tempered surface placed in a climate chamber at 293.15 K. Fig. 8(a) shows the distribution of the measured temperatures $T_{yx}[j]$. The experimental determined detector noise results in $\sigma_{T_{i,\text{detector}}} = 0.033$ K, cf. Eq. (12).

The fixed pattern noise measured after a non-uniformity correction with the camera's firmware is $\sigma_{T_{\text{pattern}}} = 0.009$ K, cf. Eq. (13). The distribution of the averaged measured temperatures $\overline{T}_{yx}$ in the image is shown in Fig. 8(b). The combined measurement uncertainty of the temperature results in $\sigma_{T_i} = \sqrt{\sigma^2_{T_{i,\text{detector}}} + \sigma^2_{T_{\text{pattern}}}} = 0.034$ K at a temperature of 293.15 K.

Based on $\sigma_{T_i} = \sigma_T = 0.034$ K, the results of the measurement uncertainty propagation for the localization of the laminar-turbulent transition are shown as a function of the total temperature difference ΔT in Fig. 9(a) and as a function of the width $8\widehat{c}$ of the transition region in Fig. 9(b). In Fig. 9(a) the width of the transition region is assumed to be $8\widehat{c} = 12$ pixels and the temperature difference ΔT is varied between 0.1 and 5 K. For Fig. 9(b) the temperature difference is fixed to $\Delta T = 1$ K and the width $8\widehat{c}$ of the transition region is varied between 2 and 100 pixels.

The estimated measurement uncertainty for the approximation of the temperature profile by the Gaussian error function shows the dependencies $\sigma_{y_{\text{tr}}} \sim \frac{1}{\Delta T}$ and $\sigma_{y_{\text{tr}}} \sim \ln\widehat{c}$. As the measurement uncertainty $\sigma_{y_{\text{tr}}}$ is additionally influenced by flow-induced temperature fluctuations, $\sigma_{y_{\text{tr}}}$ has to be determined individually for each measurement before it is propagated to $\sigma_{p_{\text{tr}}}$ and finally to $\sigma_{P_{\text{tr}}}$ and $\sigma_{\xi_{\text{tr}}}$

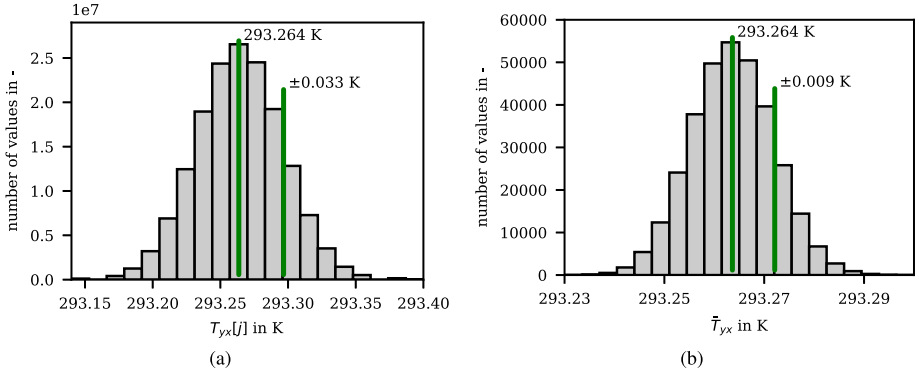

Fig. 8. Visualization of the temporal noise and the spatial noise of the used infrared camera. In (a) the temporal noise is shown. The standard deviation of the mean is the detector noise $\sigma_{T_{i,\text{detector}}} = 0.033$ K. (b) shows the spatial noise, whereas the standard deviation of the mean value is the pattern noise $\sigma_{T_{\text{pattern}}} = 0.009$ K.

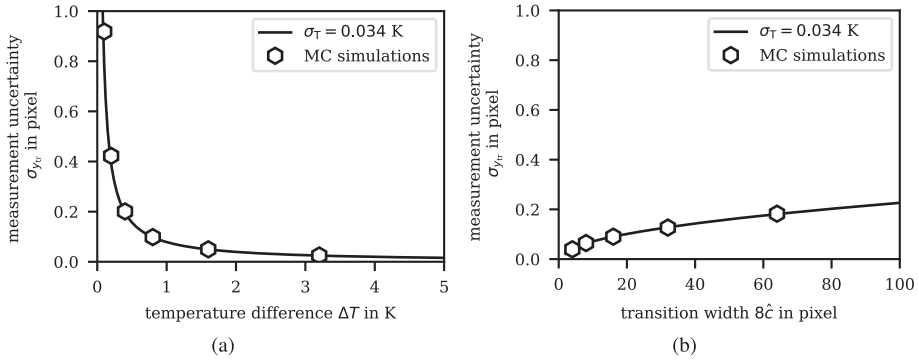

Fig. 9. Calculated measurement uncertainty $\sigma_{y_{\text{tr}}}$ of the transition position for the approximation of the temperature profile with a Gaussian error function. Fig. 9(a) shows $\sigma_{y_{\text{tr}}}$ as a function of the temperature difference ΔT between the laminar and the turbulent flow region, which is varied between 0.1 and 5 K, whereas the transition width is $8\widehat{c} = 12$ pixels. In Fig. 9(b) the transition width is varied between 2 and 100 pixels and the temperature difference is fixed to 1 K. The solid lines represent the analytical calculation and the white hexagons show the numerical results of Monte Carlo simulations (each with 10,000 runs) for verification purposes.

taking into account the uncertainty contributions of ΔX, ΔY and Θ.

The distance ΔX between the measuring position and the tower base of the wind turbine is determined by measuring both positions using the Global Positioning System (GPS) and then calculating the distance. The GPS measurements are carried out with an outdoor GPS device from the company *Garmin*. The device is equipped with a receiver that enables position determination with the European Geostationary Navigation Overlay Service (EGNOS) system. To determine the position, the measurements are repeated several times and averaged over the period of the measurement. The EGNOS-compatible receiver allows a positioning uncertainty of ±3 m (extension factor = 2) [41]. A Gaussian uncertainty propagation for the determination of the distance between two in-plane points results in a measurement uncertainty of $\sigma_{\Delta X} = \frac{3\ \mathrm{m}}{2}\sqrt{2}$.

The hub height ΔY of the investigated wind turbine is specified as 62 m. Assuming that the hub height is given to the nearest meter, an uncertainty of $\sigma_{\Delta Y} = \frac{0.5}{\sqrt{3}}$ m results for the height of the wind turbine [42].

Considering the rotor blade angle Θ, cf. Eq. (4), the pitch angle ϑ of the wind turbine blade influences the result of the geometric assignment. For this reason, the measurements presented in this work were performed on the wind turbine during operation exclusively in the partial load range (before rated power is reached). Thus, a constant blade pitch angle can be assumed without control adjustments by the blade pitch mechanism. On the basis of 10-min average values over 48 h, a blade pitch angle of 2° could be determined for the partial load range up to 800 kW. For an estimation of the uncertainty of the blade pitch angle, we refer to the *guideline for the certification of wind turbines* published by GL. Both in the version of the guideline valid at the time of installation of the wind farm and in the latest version [43], a maximum deviation of the blade angle of 0.3° from the design angle is recommended for load calculations. As no more precise information on the uncertainty of the blade pitch angle is available, the rather conservative assumption of the blade pitch angle of $\vartheta = 2^\circ \pm \frac{0.3^\circ}{\sqrt{3}}$ is used in the following, which results in $\sigma_\Theta = \frac{0.3^\circ}{\sqrt{3}}$, cf. Eq. (4).

3.2. Wind tunnel experiments

In order to determine the aerodynamic properties of the five known radial profile cuts, wind tunnel measurements were conducted. The experiments took place in the WindGuard's aeroacoustic wind tunnel in Bremerhaven, Germany. The wind tunnel is a closed-return type in which laminar flows (turbulence intensity < 0.3 %) at wind speeds of up to 100 m s^{-1} and chord Reynolds numbers of up to 6.0×10^6 can be achieved. The wind tunnel can be operated either with an open or a closed test section and is designed for acoustic and aerodynamic research. The closed test section allows testing of up to 0.9 m chord models; therefore, wind turbine airfoil segments as well as winglets can be tested at or close to a 1:1 scale. Based on the measured geometries of the five radial cuts of the rotor blade, five wind tunnel models were made of glass-fiber reinforced plastic (GFRP) with a polyurethane top coat - as it is typical for wind turbine rotor blades. In contrast to wind turbine rotor blades the inner structure of the aerodynamic model consists of a steel and aluminum frame. The models are scaled from the original chord length to 800 mm in order to fit into the wind tunnel. The aerodynamic models are mounted vertically between two turntables. The lift force is measured directly through force measurements on the turntables and indirectly through pressure measurements in the wind tunnel sidewalls. A combination of a 6 component force balance attached to the base turntable and a 2 component force balance attached to the upper turntable allows the direct measurement of the total wind forces acting on the models. Pressure measurements using independently connected high range piezo pressure sensors for each port are performed. The sensors measure in differential mode and the pressure range is from 0 to ±500 mbar at an output voltage from 0.5 to 4.5 V. The manufacturer specifies a total accuracy of ±0.5 % of the output span ±0.02 V ≙ ±5 mbar. The pressure sensors are connected to the 64 pressure taps in the wind tunnel walls. In addition, a wake rake with 52 total pressure sensors and 11 static pressure sensors is available for drag measurements in the wake of the profiles. During the measurements, temperature, pressure and humidity are measured at two locations in the wind tunnel system to determine the fluid density. The wind speed is determined with a total of four pitot tubes.

The five profile cuts from the rotor blade were tested in both clean and leading edge tripped conditions using zig-zag tape. The zig-zag tape is positioned at $x/c = 0.05$ on the suction side and $x/c = 0.10$ on the pressure side. The zig-zag tape thickness is 0.205 mm for the radial cuts r_3 to r_5 and 0.255 mm for cut r_2. Additionally, 0.4 mm thick zig-zag tape is positioned on the two outer sections at $x/c = 0.50$ pressure side, whereas it is 0.5 mm thick on the real rotor blade. Without the zig-zag tape, the boundary layer flow may be fully laminar causing a tonal noise. Fig. 10 shows the aerodynamic lift (a) and drag (b) polars of the five profile cuts. Furthermore, a zig-zag tape applied to the surface of the wind tunnel model is shown in Fig. 10(c).

Again, for the protection of the internal knowledge of the manufacturer, the ordinate was not labeled to give only qualitative information.

3.3. BEM simulation model

For the estimation of the AEP, a BEM model of the *GE* 1.5 MW wind turbine is constructed using the open-source code *Qblade* (v0.96). In addition to using the Prandtl tip and root loss corrections, a 3D polar correction by Snel et al. is applied [44]. The rotor blade shape is defined by the previously measured five radial profile cuts and the cylindrical root of the blade. Between the known geometries, an interpolation takes place. The wind turbine rotor rpm was measured during the thermographic measurements in field by the optical trigger system, which enabled the creation of a wind speed vs. rpm curve for use in the BEM simulation. Baseline BEM calculations are carried out using the clean condition wind tunnel polars to obtain a power curve of a rotor without contamination or erosion of the leading edge. The baseline BEM power curve values are within 10 % of those seen in field test data for this type of wind turbine and for the wind speeds used for the analysis in this paper. As the aim is to calculate representative performance deltas and not to create the most accurate wind turbine model, these differences are considered acceptable for the purposes of the study. In order to generate a power curve for heavy contamination conditions, the BEM simulation is repeated replacing the outer three clean airfoil polars, that represent roughly 50 % of the rotor blade length and over 60 % of the swept surface, with the leading edge tripped aerodynamic polars measured in the wind tunnel.

In addition to the aerodynamic wind tunnel data, the well-known software *Xfoil* (v6.97) was used to determine the change in lift and drag polars due to the presence of leading edge contamination by fixing the transition position to the field measurement results $p_{\mathrm{tr,act}}$ and $p_{\mathrm{tr,nat}}$, respectively. The deltas are applied to the clean condition wind tunnel polars and the BEM simulation is run again with these polars to obtain power curves for the specific contamination conditions.

The AEP for all considered conditions was calculated within

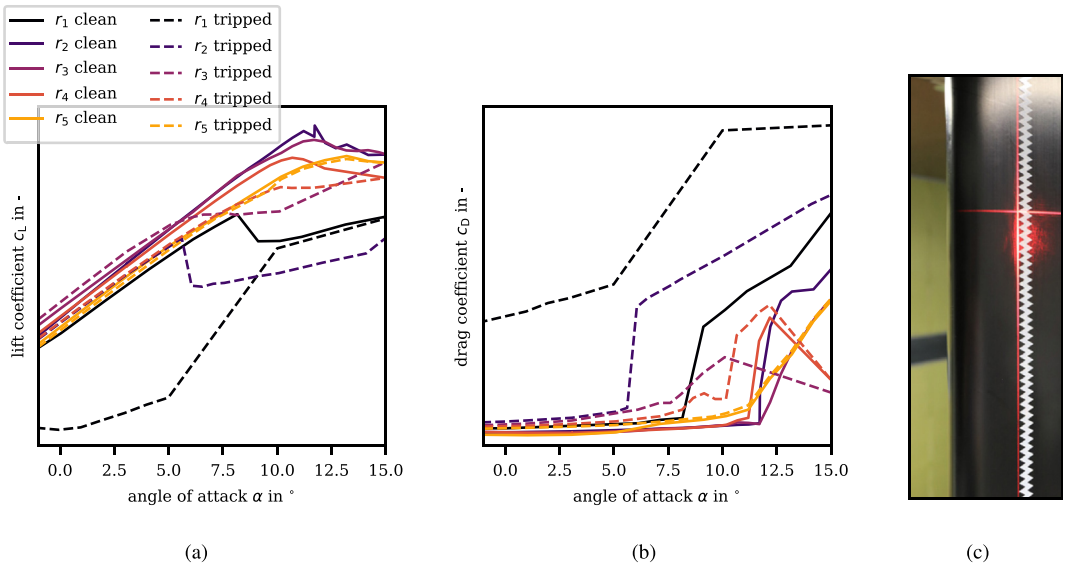

Fig. 10. Aerodynamic measurements of the five known radial profile cuts measured in the Deutsche WindGuard's aero-acoustic wind tunnel in Bremerhaven, Germany, both in clean and leading edge tripped conditions. Aerodynamic polar of (a) the lift coefficient c_L and (b) the drag coefficient c_D over the angle of attack α as well as (c) the applied zig-zag tape used for the tripping.

Qblade using a Weibull *k*-factor of 2 and average wind speeds of 6 m/s, 7.5 m/s, 8 m/s, and 9 m/s. When the outer airfoils were fully tripped the estimated AEP loss compared to the clean rotor blade was between 6.1 % and 3.9 % for the analyzed wind speeds between 6 m/s and 9 m/s. The AEP loss is highest (6.1 %) when the site average wind speed is lowest (6 m/s) because the turbine spends more time in the partial load region of operation where changes in c_L and c_D directly impact power (unlike after rated power has been reached where they no longer have an influence).

The described methodology is based on the assumption that the contamination of the leading edge is not subject to a seasonal fluctuation and that the erosion captured at the time of the measurement does not progress. In fact, the contamination will vary with the environmental conditions and precipitation frequency, and erosion increases progressively; however, since the current industrial standard is to use only clean and tripped aerodynamic polars to evaluate the impact of erosion or contamination, the process can be greatly enhanced through the use of real field-measured data.

4. Thermographic measurement of the LEC

Fig. 11 shows the thermographic measurement results of two different LEC cases captured on different days with different weather conditions. Both images are composed of instantaneous single frames, with one thermographic image taken every rotation of the rotor. In Fig. 11(a) a thermographic image of a relatively clean rotor blade suction side is shown (1st case). The measurement distance is 180 m. In contrast, Fig. 11(b) shows a heavily contaminated suction side of the *LM 37.3p* rotor blade with a measurement distance of 110 m (2nd case). The different distances result in image diagonals of (a) 12.4 m and (b) 7.6 m. The positions $P_{tr,act}$ and $P_{tr,nat}$ of the actual and the natural transition determined by the image processing presented in Sect. 2 are indicated by dashed and solid

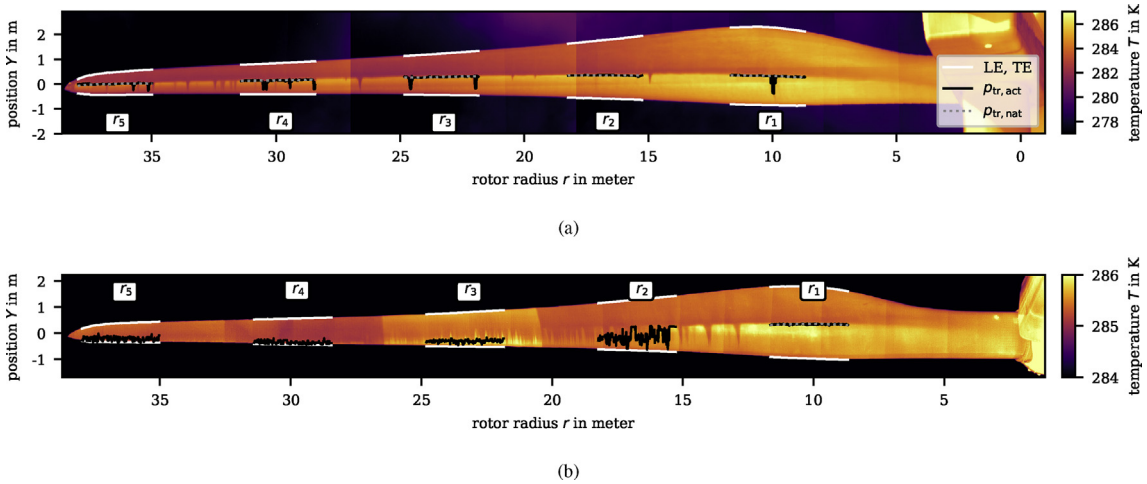

Fig. 11. LEC measurements on the suction side of the rotor blade with a rotor radius of 38.5 m in two different conditions. (a) Thermographic measurement results from a working distance of 180 m with an exceptionally clean rotor blade (1st case). (b) Thermographic image of the same rotor blade from a working distance of 110 m with a significant degree of leading edge contamination (2nd case). The results at the five radial sections r_i, $i = 1, \ldots, 5$ are summarized for both cases in Table 1 and Table 3.

lines, respectively. Especially in the first image, additional temperature gradients can be identified apart from the laminar-turbulent transition. These visible lines are caused by the inner structure of the rotor blade (in this case the belt) and not by the boundary layer flow. The image processing takes place for each radial section in a region of ±1.5 m around the known radial profile cuts. For the 1st case there has been an additional measurement of the pressure side from a measurement distance of 250 m with a maximum of $\xi_{tr} = 3.2$ %. The measurement of the pressure side is not shown, but considered in the following evaluation of the AEP.

The transition location measured in the 1st case is assumed to correspond to the natural transition location. As it is unknown to the authors if the surface roughness of this rotor blade has varied since its manufacturing date, ξ_{tr} is measured in relative terms. The results for $P_{tr,act}$, $P_{tr,nat}$ and ξ_{tr} as well as the associated measurement uncertainties for the 1st case are summarized in Table 1.

The measurement uncertainty of the relative position $\sigma_{p_{tr,act}}$ in the thermographic image is determined by Eq. (15), whereas the measurement uncertainty estimation for $\sigma_{y_{tr}}$ is presented in Sect. 2.1.2. Furthermore the flow induced temperature fluctuations are considered in terms of a spatial noise. For the determination of $\sigma_{y_{tr}}$, the width of the transition region and the measured temperature difference were determined manually for each column. In the case of the measurement uncertainty for the position of the natural transition $\sigma_{p_{tr,nat}}$ a manual preselection of the transition positions took place previously to calculate the standard uncertainty of the mean; the transition positions at the site of turbulence wedges were not considered. In contrast to the determination of the natural transition using a weighted linear regression, this procedure is not suitable for an automated evaluation approach; however, at this point it enables a statement on the uncertainty of the natural transition position and thus, a statement on the overall uncertainty of ξ_{tr}.

The measurement uncertainties for the relative positions $P_{tr,act}$ and $P_{tr,nat}$ with respect to the chord length are determined by Monte Carlo simulations with 10,000 runs for each uncertainty influence. In addition to the uncertainty of the relative transition positions $p_{tr,act}$ and $p_{tr,nat}$ in the thermographic image, other uncertainty influences discussed previously in Sect. 2.1.3 and section 3 contribute to the measurement uncertainty budget. As an example, the measurement uncertainty budget for $P_{tr,act}$ is shown in Table 2.

The measurement uncertainty of the relative position ($p_{tr,act}$ or $p_{tr,nat}$) of the transition in the thermographic image increases towards the tip of the rotor blade due to the smaller depth between the visible leading and trailing edge and due to the increasing number of turbulence wedges. The temperature gradient at the wedges is significantly lower compared to transition positions which can be assigned to the natural transition due to the shape as well as due to the position shifted towards the leading edge. Although the number of individual transition positions available for averaging is smaller, the uncertainty of the position of the natural transition is lower than the uncertainty of the position of the actual transition. This can be explained by the increased measurement uncertainty at turbulence wedges.

Table 2
Measurement uncertainty budget for the position $P_{tr,act}$ of the actual transition on the suction side of the rotor blade shown in Fig. 11(a) (1st case).

influence	rotor blade section around radial profile				
	r_1	r_2	r_3	r_4	r_5
$\sigma_{P_{tr,act},p_{tr,act}}$	0.000	0.000	0.000	0.001	0.001
$\sigma_{P_{tr,act},\Delta X}$	0.001	0.001	0.001	0.001	0.001
$\sigma_{P_{tr,act},\Delta Y}$	0.000	0.000	0.000	0.000	0.000
$\sigma_{P_{tr,act},\Theta}$	0.001	0.001	0.001	0.000	0.000
$\sigma_{P_{tr,act}}$	0.001	0.001	0.001	0.001	0.001

Fig. 11(b) shows a rotor blade of the same type with a significant degree of leading edge contamination in the outer half. The measurement distance for this measurement is 110 m. The evaluation of ξ_{tr} results in a maximum of 90.4 % at the radial section r_4. Due to the high number of turbulence wedges in the outer region of the rotor blade, a determination of the natural transition position $P_{tr,nat}$ is not possible. Instead, the individual $P_{tr,nat}$ of the 1st case around the radial profiles $r_i, i = 2, \ldots, 5$ are used as a reference. This seems to be applicable since the positions of the natural transition around profile r_1 are nearly the same in both cases.

Similar to the results of the relatively clean 1st case, Table 3 shows the results for the heavily contaminated 2nd case. Due to the higher number of turbulence wedges and the corresponding higher measurement uncertainty of the actual transition position $P_{tr,act}$, the measurement uncertainty of ξ_{tr} is higher compared to the 1st case.

5. Calculation of the AEP

For the calculation of the AEP, shifts of the transition position on both the suction and pressure side were considered in the 1st case condition. In the 2nd case only the suction side was considered. This is due to the available data and due to the fact that the pressure side is tripped at 50 %, which reduces the possible impact of a pressure side contamination. A contamination as well as a tripping leads to a premature laminar-turbulent transition. Tripping at $0.5\,x/c$ accordingly reduces the influence of a possible contamination at the leading edge of the rotor blade compared to a natural transition further back on the chord.

Each radial aerodynamic profile's performance was analyzed at its operational angle of attack (taken from the BEM results in the constant pitch partial-load operating region) before manually setting a transition location further forward by the amount determined through on-site thermography. This allows the calculation of performance deltas that can be applied to the measured aerodynamic polars. Fig. 12 shows the aerodynamic polars of the radial profile r_5 for all four cases, clean and leading edge tripped conditions as well as modified for the 1st and 2nd case leading edge

Table 1
Extent ξ_{tr} of boundary layer flow affected by erosion or contamination for the relatively clean 1st case at the five radial positions $r_i,\ i = 1, \ldots, 5$ based on the comparison of the determined actual and the natural transition positions $P_{tr,act}$ and $P_{tr,nat}$.

	rotor blade section around radial profile				
	r_1	r_2	r_3	r_4	r_5
$P_{tr,act}$	0.338 ±0.001	0.356 ±0.001	0.381 ±0.001	0.384 ±0.001	0.426 ±0.001
$P_{tr,nat}$	0.346 ±0.001	0.357 ±0.001	0.393 ±0.001	0.405 ±0.001	0.442 ±0.001
ξ_{tr}	2.3 %±0.0 %	0.1 %±0.1 %	3.0 %±0.1 %	5.2 %±0.1 %	3.6 % ± 0.2 %

Table 3
Extent ξ_{tr} of boundary layer flow affected by erosion or contamination for the highly contaminated 2nd case at the five radial positions r_i, $i = 1, \ldots, 5$ based on the comparison of $P_{tr,act}$ and $P_{tr,nat}$.

	rotor blade section around radial profile				
	r_1	r_2	r_3	r_4	r_5
$P_{tr,act}$	0.340 ±0.000	0.154 ±0.001	0.090 ±0.002	0.039 ±0.004	0.129 ±0.009
$P_{tr,nat}$	0.340 ±0.001	0.357 ±0.001	0.393 ±0.001	0.405 ±0.001	0.442 ±0.001
ξ_{tr}	0.0 %±0.2 %	56.9 %±0.7 %	76.4 %±0.6 %	90.4 %±1.0 %	70.8 %±2.0 %

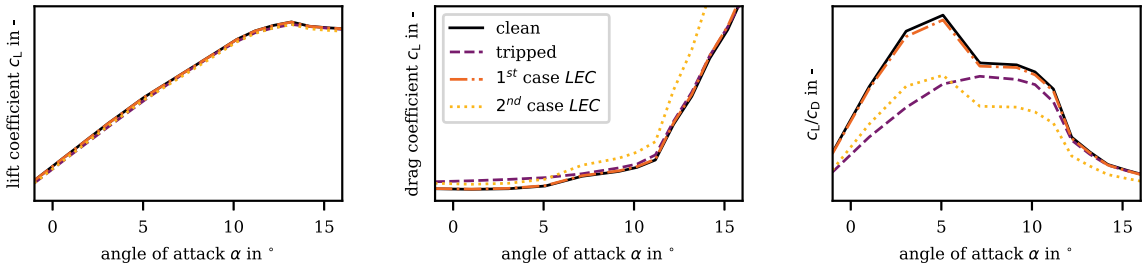

Fig. 12. Aerodynamic polars of the radial profile r_5 in clean and leading edge tripped conditions as well as modified for the 1st and 2nd case leading edge contamination conditions. (a) Lift coefficient c_L, (b) drag coefficient c_D and (c) c_L/c_D as a function of the angle of attack α.

contamination conditions.

The performance deltas calculated by *Xfoil* and applied to the measured aerodynamic polars for each profile cut for the 1st case and the 2nd case are shown in Table 4 and Table 5, respectively. For the 1st case, the calculated performance deltas are very small due to the marginal shift in transition position caused by contamination and erosion. In contrast to the 1st case, the aerodynamic performance losses for the 2nd case are significant.

The modified aerodynamic polars replace the corresponding clean polars in the BEM simulation. The global wind turbine parameters are not changed in comparison to the baseline cases. Fig. 13 shows the c_L/c_D vs. rotor blade radius r curve for all four cases.

Due to the low leading edge contamination present in most rotor blade root regions, the difficulty of measuring thick airfoil sections in the wind tunnel and the associated uncertainty in measured performance, it was decided not to include the inner two airfoils ($r \leq 17.05$ m) in their tripped state. Obviously both leading edge contamination cases reduce the rotor blade c_L/c_D. The relatively clean 1st case only slightly reduces the c_L/c_D, whereas the heavily contaminated 2nd case reduces c_L/c_D by similar degrees to the fully tripped condition by the application of zig-zag tape.

The estimated AEP loss for the three other cases is compared against the clean case in Table 6. The very small amount of leading edge contamination measured by thermographic flow visualization in the 1st case results in a marginal AEP loss of 0.2 %–0.1 % or 7 MWh to 8 MWh, respectively. In reality it would be difficult to measure an AEP loss of this low magnitude because the delta would be within the uncertainty of the measurement. For the 2nd case, the heavy leading edge contamination results in AEP losses between 4.7 % and 2.7 %, which corresponds to 143 MWh to 171 MWh for the investigated average wind speeds between 6 m/s and 9 m/s. The comparison with the tripped case indicates that the AEP loss of the heavily contaminated case is still far below the leading edge tripped case. This result reinforces the statement that this work can enhance the current industry-standard practice of analyzing a binary clean/dirty state by allowing the assessment of the intermediate cases found in the real world.

Table 4
1st case measured LEC and aerodynamic performance deltas evaluated with *Xfoil*.

profile	SS ξ_{tr}	PS ξ_{tr}	Δc_L	Δc_D
r_1	2.3 %	0.0 %	−1.0 %	+3.0 %
r_2	0.3 %	0.0 %	0.0 %	0.0 %
r_3	3.0 %	0.4 %	−0.4 %	+4.0 %
r_4	5.2 %	3.2 %	−0.2 %	+4.0 %
r_5	3.6 %	2.0 %	−0.1 %	+2.0 %

Table 5
2nd case measured LEC and aerodynamic performance deltas evaluated with *Xfoil*.

profile	SS ξ_{tr}	PS ξ_{tr}	Δc_L	Δc_D
r_1	0.0 %	–	−0.1 %	+0.2 %
r_2	56.9 %	–	−2.0 %	+45.0 %
r_3	76.4 %	–	−4.0 %	+75.0 %
r_4	90.4 %	–	−9.0 %	+70.0 %
r_5	70.8 %	–	−6.0 %	+45.0 %

6. Conclusions and outlook

In order to quantify the extent of the boundary layer flow disturbed by contamination or erosion of the rotor blade leading edge, thermographic flow visualization measurements were performed. The measurement results were used to estimate the impact of the LEC on the AEP. In contrast to the industry standard of using both clean and tripped aerodynamic polars in simulations to analyze two binary extreme operating conditions, the presented approach enhances the methodology by including more representative real world data.

Thermographic flow visualization measurements post-processed using image processing algorithms enable a non-invasive localization of the actual laminar-turbulent transition position influenced by the LEC and in most conditions the natural transition position adjusted for turbulence wedges. The signal

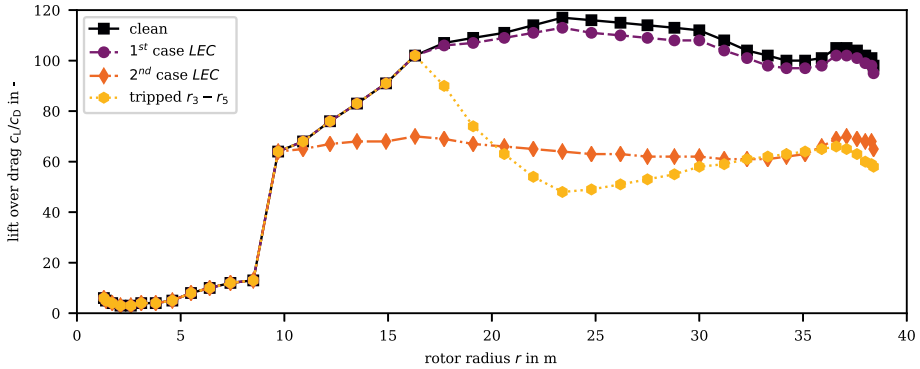

Fig. 13. Lift over drag c_L/c_D as a function of the rotor blade radius r for all four conditions: clean, tripped, 1st and 2nd case leading edge contamination. For the tripped condition r_1 and r_2 are not considered due to the difficulties of measurements of thick airfoils in wind tunnel experiments.

Table 6
AEP loss for the 3 cases, 1st case leading edge contamination, 2nd case leading edge contamination and tripped compared to the clean case. The results for the AEP loss are given for average wind speeds of 6 m/s, 7.5 m/s, 8 m/s and 9 m/s.

condition	AEP loss at 6 m/s		AEP loss at 7.5 m/s		AEP loss at 8 m/s		AEP loss at 9 m/s	
	in %	in MWh	in %	in MWh	in %	in MWh	in %	in MWh
clean	–	–	–	–	–	–	–	–
1st case	0.2	7	0.2	8	0.2	8	0.1	8
2nd case	4.7	143	3.6	171	3.3	173	2.7	171
tripped	6.1	186	4.9	235	4.6	242	3.9	245

processing approach used permits the localization with a measurement uncertainty in the subpixel range depending on the available thermal contrast and the transition width. A geometric assignment of the two-dimensional image data to the three-dimensional geometry of the rotor blade by taking into account additional knowledge about the measurement situation allows chord-based location information to be given with a measurement uncertainty of up to 0.1 % of the chord length.

A quantification of the extent of the boundary layer flow influenced by a degraded leading edge due to contamination or erosion can be achieved by comparing both the natural (clean) and the actual (contaminated) transition position. The extent of affected boundary layer flow ξ_{tr} is defined as the difference between the natural and the actual transition position $P_{tr,nat}$ and $P_{tr,act}$ normalized by the natural transition position.

The positions of the actual and the natural laminar-turbulent transition are used as an input for a simulation to estimate the power performance change due to different leading edge conditions. For this purpose, aerodynamic polar measurements were modified using the field measurements on a multi-MW wind turbine and *Xfoil* simulations. The modified polars were subsequently used within a BEM simulation to estimate the AEP.

Both a relatively clean case and a heavily contaminated case of a 37.3 m rotor blade from a 1.5 MW wind turbine were analyzed. The clean case shows an average boundary layer impact of 2.8 % and a maximum of 5.2 % resulting in an AEP loss of less than 0.2 % for the investigated average wind speeds between 6 m/s and 9 m/s. In contrast to the clean case, the heavily contaminated case shows an average boundary layer impact of 58.9% and a maximum of 90.4 %. This results in a significant AEP loss between 4.7 % and 2.7 % for the investigated average wind speeds, which is equivalent to an energy loss of up to 245 MWh.

The presented methodology can be used as the basis for an automated method to assess the need for rotor blade cleaning or repair based on the individual wind turbine's economic case. Furthermore, based on a statistical evaluation, the method can be used to obtain more reliable data on the AEP influence of seasonal and progressing leading edge contamination. For this reason, future work should be a long-term field measurement campaign to capture the measured seasonal impact of boundary layer flow disturbances due to contamination and to correlate this information with the environmental conditions and performance data of the wind turbine. This will provide a deeper understanding of the performance losses due to the LEC.

Acknowledgements

The authors gratefully acknowledge the financial support by the German Federal Environmental Foundation (Grant no. 27118) and the Bremerhaven Economic Development Company with a funding of the state of Bremen (Grant no. 59203). *InfraTec* is gratefully acknowledged for the technical support during the experiments for this work.

References

[1] W. Han, J. Kim, B. Kim, Effects of contamination and erosion at the leading edge of blade tip airfoils on the annual energy production of wind turbines, Renew. Energy 115 (2018) 817–823, https://doi.org/10.1016/j.renene.2017.09.002.
[2] G.P. Corten, H.F. Veldkamp, Insects can halve wind-turbine power, Nature 412 (2001) 41, https://doi.org/10.1038/35083698.
[3] N. Dalili, A. Edrisy, R. Carriveau, A review of surface engineering issues critical to wind turbine performance, Renew. Sustain. Energy Rev. 13 (2) (2009) 428–438, https://doi.org/10.1016/j.rser.2007.11.009.
[4] M.H. Keegan, D.H. Nash, M.M. Stack, On erosion issues associated with the leading edge of wind turbine blades, J. Phys. Appl. Phys. 46 (38) (2013), 383001, https://doi.org/10.1088/0022-3727/46/38/383001.
[5] H. Slot, E. Gelinck, C. Rentrop, E. van der Heide, Leading edge erosion of coated wind turbine blades: review of coating life models, Renew. Energy 80 (2015) 837–848, https://doi.org/10.1016/j.renene.2015.02.036.
[6] E. Sagol, M. Reggio, A. Ilinca, Issues concerning roughness on wind turbine blades, Renew. Sustain. Energy Rev. 23 (2013) 514–525, https://doi.org/10.1016/j.rser.2013.02.034.
[7] N. Gaudern, A practical study of the aerodynamic impact of wind turbine blade leading edge erosion, J. Phys. Conf. 524 (1) (2014), 012031, https://doi.org/10.1088/1742-6596/524/1/012031.
[8] W.S. Coleman, The characteristics of roughness from insects as observed for two-dimensional, incompressible flow past airfoils, J. Aero. Sci. 26 (5) (1959) 264–280, https://doi.org/10.2514/8.8044.
[9] W.A. Timmer, A.P. Schaffarczyk, The effect of roughness at high Reynolds numbers on the performance of aerofoil DU 97-W-300Mod, Wind Energy 7 (4) (2004) 295–307, https://doi.org/10.1002/we.136.
[10] R. Schaefer Ehrmann, E.B. White, D.C. Maniaci, R. Chow, C. Langel, C.P. Van Dam, Realistic leading-edge roughness effects on airfoil performance, in: 31st AIAA Applied Aerodynamics Conference, AIAA, 2013, https://doi.org/10.2514/6.2013-2800.
[11] A. Sareen, C.A. Sapre, M.S. Selig, Effects of leading edge erosion on wind turbine blade performance, Wind Energy 17 (10) (2014) 1531–1542, https://

doi.org/10.1002/we.1649.
[12] M. Kok, T. Mertens, D. Raps, T.M. Young, Influence of surface characteristics on insect residue adhesion to aircraft leading edge surfaces, Prog. Org. Coating 76 (11) (2013) 1567–1575, https://doi.org/10.1016/j.porgcoat.2013.06.013.
[13] P. Gigure, M.S. Selig, Aerodynamic effects of leading-edge tape on aerofoils at low Reynolds numbers, Wind Energy 2 (3) (1999) 125–136, https://doi.org/10.1002/(sici)1099-1824(199907/09)2:3<125::aid-we23>3.0.co;2-5.
[14] A. Sareen, C.A. Sapre, M.S. Selig, Effects of leading-edge protection tape on wind turbine blade performance, Wind Eng. 36 (5) (2012) 525–534, https://doi.org/10.1260/0309-524X.36.5.525.
[15] A.P. Schaffarczyk, D. Schwab, M. Breuer, Experimental detection of laminar-turbulent transition on a rotating wind turbine blade in the free atmosphere, Wind Energy 20 (2) (2017) 211–220, https://doi.org/10.1002/we.2001.
[16] D.M. Eggleston, K. Starcher, A comparative study of the aerodynamics of several wind turbines using flow visualization, J. Sol. Energy Eng. 112 (4) (1990) 301–309, https://doi.org/10.1115/1.2929938.
[17] N. Swytink-Binnema, D.A. Johnson, Digital tuft analysis of stall on operational wind turbines, Wind Energy 19 (4) (2016) 703–715, https://doi.org/10.1002/we.1860.
[18] I. Zidane, K. Saqr, G. Swadener, X. Ma, M. Shehadeh, On the role of surface roughness in the aerodynamic performance and energy conversion of horizontal wind turbine blades: a review, Int. J. Energy Res. 40. https://doi.org/10.1002/er.3580.
[19] L. de Luca, G.M. Carlomagno, G. Buresti, Boundary layer diagnostics by means of an infrared scanning radiometer, Exp. Fluid 9 (3) (1990) 121–128, https://doi.org/10.1007/BF00187411.
[20] E. Gartenberg, A.S. Roberts, Airfoil transition and separation studies using an infrared imaging system, J. Aircraft 28 (4) (1991) 225–230, https://doi.org/10.2514/3.46016.
[21] E. Gartenberg, A.S. Roberts, Twenty-five years of aerodynamic research with infrared imaging, J. Aircraft 29 (2) (1992) 161–171, https://doi.org/10.2514/3.46140.
[22] L. de Luca, G. Guglieri, G. Cardone, G.M. Carlomagno, Experimental analysis of surface flow on a delta wing by infrared thermography, AIAA J. 33 (8) (1995) 1510–1512, https://doi.org/10.2514/3.12574.
[23] A.D. Gardner, C. Eder, C.C. Wolf, M. Raffel, Analysis of differential infrared thermography for boundary layer transition detection, Exp. Fluid 58 (9) (2017) 122, https://doi.org/10.1007/s00348-017-2405-z.
[24] E. Gartenberg, R.E. Wright, Boundary-layer transition detection with infrared imaging emphasizing cryogenic applications, AIAA J. 32 (9) (1994) 1875–1882, https://doi.org/10.2514/3.12186.
[25] A. Séraudie, J. Perraud, F. Moens, Transition measurement and analysis on a swept wing in high lift configuration, Aero. Sci. Technol. 7 (8) (2003) 569–576, https://doi.org/10.1016/j.ast.2003.04.001.
[26] L.A. Joseph, A. Borgoltz, W. Devenport, Infrared thermography for detection of laminar-turbulent transition in low-speed wind tunnel testing, Exp. Fluid 57 (5) (2016) 77, https://doi.org/10.1007/s00348-016-2162-4.
[27] S. Montelpare, R. Ricci, A thermographic method to evaluate the local boundary layer separation phenomena on aerodynamic bodies operating at low Reynolds number, Int. J. Therm. Sci. 43 (3) (2004) 315–329, https://doi.org/10.1016/j.ijthermalsci.2003.07.006.
[28] M. Raffel, C.B. Merz, T. Schwermer, K. Richter, Differential infrared thermography for boundary layer transition detection on pitching rotor blade models, Exp. Fluid 56 (2) (2015) 30, https://doi.org/10.1007/s00348-015-1905-y.
[29] A.D. Gardner, C.C. Wolf, M. Raffel, A new method of dynamic and static stall detection using infrared thermography, Exp. Fluid 57 (9) (2016) 149, https://doi.org/10.1007/s00348-016-2235-4.
[30] S. von Hoesslin, M. Stadlbauer, J. Gruendmayer, C.J. Kähler, Temperature decline thermography for laminar-turbulent transition detection in aerodynamics, Exp. Fluid 58 (9) (2017) 129, https://doi.org/10.1007/s00348-017-2411-1.
[31] C. Dollinger, N. Balaresque, M. Sorg, A. Fischer, IR thermographic visualization of flow separation in applications with low thermal contrast, Infrared Phys. Technol. 88 (2018) 254–264, https://doi.org/10.1016/j.infrared.2017.12.001.
[32] B.K. Crawford, G.T. Duncan, D.E. West, W.S. Saric, Robust, automated processing of IR thermography for quantitative boundary-layer transition measurements, Exp. Fluid 56 (7) (2015) 149, https://doi.org/10.1007/s00348-015-2011-x.
[33] K. Richter, E. Schülein, Boundary-layer transition measurements on hovering helicopter rotors by infrared thermography, Exp. Fluid 55 (7) (2014) 1755, https://doi.org/10.1007/s00348-014-1755-z.
[34] C. Dollinger, M. Sorg, N. Balaresque, A. Fischer, Measurement uncertainty of IR thermographic flow visualization measurements for transition detection on wind turbines in operation, Exp. Therm. Fluid Sci. 97 (2018) 279–289, https://doi.org/10.1016/j.expthermflusci.2018.04.025.
[35] D. Traphan, I. Herráez, P. Meinlschmidt, F. Schlüter, J. Peinke, G. Gülker, Remote surface damage detection on rotor blades of operating wind turbines by means of infrared thermography, Wind Energy Sci. 3 (2) (2018) 639–650, https://doi.org/10.5194/wes-3-639-2018.
[36] S. Briot, W. Khalil, Homogeneous transformation matrix, in: Dynamics of Parallel Robots, Springer International Publishing, 2015, pp. 19–32, https://doi.org/10.1007/978-3-319-19788-3_2.
[37] S.M. Kay, Fundamentals of Statistical Signal Processing, Prentice Hall, 1993.
[38] J.N. Sørensen, General Momentum Theory for Horizontal Axis Wind Turbines, Springer International Publishing, 2016, https://doi.org/10.1007/978-3-319-22114-4.
[39] M. Drela, XFOIL: an analysis and design system for low Reynolds number airfoils, in: Low Reynolds Number Aerodynamics: Proceedings of the Conference Notre Dame, 1989, pp. 1–12, https://doi.org/10.1007/978-3-642-84010-4_1.
[40] N. Balaresque, S. Bicker, C. Dollinger, A. Fandrich, S. Gatz, M. Hölling, K. Irschik, T. Reichstein, A.P. Schaffarczyk, C. von Zengen, Investigations for improvement of energy yield of rotor-blades from the 1.5 MW class, J. Phys. Conf. 753 (7) (2016), 072012, https://doi.org/10.1088/1742-6596/753/7/072012.
[41] European Global Navigation Satellite Systems Agency, EGNOS Safety of Life (SoL) Service Definition Document, Techreport, European Global Navigation Satellite Systems Agency (GSA), 2016.
[42] International Organization for Standardization, Guide to the Expression of Uncertainty in Measurement, 2008.
[43] G.L. Germanischer Lloyd Industrial Services GmbH, Guideline for the Certification of Wind Turbines, 2010.
[44] H. Snel, R. Houwking, G.J.W. van Bussel, A. Bruining, Sectional prediction of 3D effects for stalled flow on rotating blades and comparison with measurements, in: Proc. of the European Community Wind Energy Conference, H.S. Stevens and Associates, Lübeck Travemünde, 1993.